Structural Monitoring and Maintenance, *Vol. 12, No. 3 (2025) 231-257*
https://doi.org/10.12989/smm.2025.12.3.231

State-of-the-art structural health monitoring for reinforced concrete structures: Advances in acoustic emission and digital image correlation

Gaurav Sharma*[1], Payal Sachdeva[2] and Divyashree Yadav[3]

[1]*Department of Civil Engineering, Lingayas Vidyapeeth, Faridabad, Haryana-121002, India*
[2]*Department of Civil Engineering, Chitkara University, Rajpura, Punjab-140401, India*
[3]*Dean of Studies, Techno strut, gurgaon, Haryana-121003, India*

(*Received November 26, 2024, Revised April 1, 2025, Accepted April 12, 2025*)

Abstract. The fundamental issue with steel-reinforced concrete constructions is corrosion of the steel bars, which finally leads to the structure's collapse and disintegration. Fiber-reinforced polymer (FRP) bars have been widely used in civil engineering used as a substitute for steel reinforcement because it has many advantages such as high strength, light weight, and no corrosion. Moreover, productive technology is becoming more and more mature and industrialized so FRP has become one economic and competitive structure material. Based on the recent research: this paper mainly introduces progress in the studies on concrete structures reinforced with steel or GFRP bars. The contents of this review research article include the cracking/fracture/cracking monitoring of Steel and GFRP reinforced concrete beams in flexure is investigated in the past few years in the world. The possibility of employing Acoustic Emission (AE) and Digital Image Correlation (DIC) to monitor micro and macro cracks generated in reinforced concrete beams will be investigated in this work so that a practical application can be presented. Finally, the integrated technique delivers complimentary information from 'the ear' with the AE and 'the eye' with the DIC.

Keywords: acoustic emission; crack widths; digital image processing; hits; steel and GFRP bars

1. Introduction

Corrosion of reinforcing steel bars is now well recognised as one of the most common and major causes of concrete building degradation across the world. (Hansson 1995). Conventional steel bars in Reinforced Concrete (RC) structures rust easily, compromising the structure's safety and serviceability (El-Maaddawy 2005). In humid conditions, contaminants from the environment penetrate the concrete cover and cause steel corrosion, reducing the strength, load-bearing capability, lifespan, and cost of RC structures (Dhawan *et al*. 2019). Two basic mechanisms cause rebar corrosion: chloride ion intrusion and carbonation of reinforced concrete structures. Corrosion occurs in reinforced concrete structures when chloride ions enter concrete beyond the threshold value or when carbonation penetration surpasses the concrete cover, resulting in rebar delamination from the surrounding concrete (Francois and Maso 1988). It creates massive

*Corresponding author, Assistant Professor, E-mail: dr.gaurav@lingayasvidyapeeth.edu.in

http://www.techno-press.org/?journal=smm&subpage=7 ISSN: 2288-6605 (Print), 2288-6613 (Online)

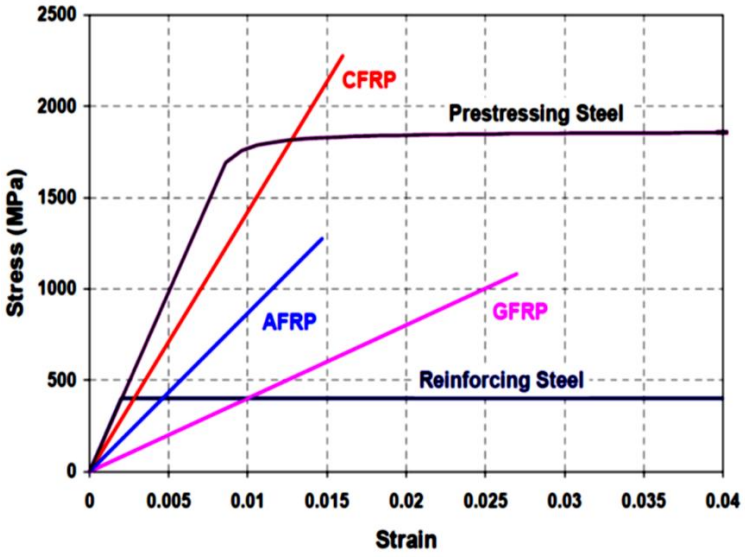

Fig. 1 Stress-strain conduct for FRP and reinforcing steel (ACI Committee 2015)

corrosion products with a volume 6-10 times that of the surrounding parent steel, causing the surrounding concrete to fracture and spalling (Castel *et al.* 2000). Additionally, various environmental degradation factors such as moisture, chemical products, freeze-thaw, de-icing salts, and marine environments speed up the corrosion mechanism of steel bars in concrete assemblies (Francois and Maso 1988).

Many tactics and methods for delaying the beginning and advancement of corrosion in RC structures have been proposed to save maintenance expenditures. Stainless steel is frequently recommended as a strategy (Rabi *et al.* 2019) and epoxy-coated rebars (Manning 1996) in place of conventional steel bars, admixing corrosion inhibitors (El-Hacha *et al.* 2010), using self-healing compounds in concrete (Stankiewicz *et al.* 2013) and use of polymer concrete (Allahvirdizadeh *et al*. 2011). The use of stainless-steel bars as reinforcement is ineffective since these bars are prone to corrosion in a harsh environment and are also expensive (Manning 1996). Over time, epoxy-coated bars lose their adherence to the concrete around them. Corrosion inhibitors in concrete slow the rate of diffusion of reactants by absorbing ions at the concrete surface, delaying but not completely preventing corrosion. Some researchers have recently proposed using self-healing micro-capsules to protect metals against corrosion (Stankiewicz *et al.* 2013). These compounds have the intrinsic potential to heal the substrate and restore functioning after deterioration, injury, or failure. However, because self-healing-based micro-capsules rupture during concrete mixing, this technology has practical limitations. Aside from that, these specific solutions are not cost-effective in structural applications and have scaling concerns.

In many civil engineering applications, Fibre-Reinforced Polymer (FRPs) composites reinforcement has been introduced in recent decades as an alternative and/or replacement material to replace traditional reinforcing steel, thereby reducing the corrosion problem. (Alsayed 1998, Mancusi and Spadea 2010, Adam *et al*. 2015, Saleh *et al.* 2019). Although other fibres such as asbestos, paper, and wood have been used in the past, aramid, basalt, carbon, and glass are the

most prevalent nowadays. Thermoset resins, such as polyester and vinylester, and thermoplastic resins, such as nylon, polyethylene, and terephthalate, are often utilised (Hensher 2016). Furthermore, FRPs are commonly used for structural applications as well as repair and rehabilitation in the aerospace, automotive, marine, and construction industries due to their cost-effectiveness and high strength properties. Glass Fibre Reinforced Polymer (GFRP) bars or sheets are commonly used in the aerospace, automotive, marine, and construction industries. FRP composites have been used as internal reinforcement in RC structures, bridges, and piers, as well as exterior reinforcement in current construction and restoration of structures for strengthening and seismic upgrading, due to these advantages. (Mancusi and Spadea 2010).

Being non-corrosive, GFRP composite bars offer numerous benefits, including electric and magnetic neutrality, convenience of handling, high strength/weight ratio high and longitudinal tensile strength as shown Fig. 1. They also are simple to construct and can be tailored to meet specific performance requirements (Goldston *et al.* 2016). Wharves, box culverts, dry docks, sea walls, floating piers, facades, and retaining walls may all benefit from GFRP bars, which can be used instead of steel rebars in severe settings like coastal areas (Goldston *et al.* 2017). In RC constructions that prevent the use of steel bars, such as magnetic resonance imaging chambers in hospitals and bridge decks near electronic toll plazas, it has been suggested that GFRP be used as concrete reinforcement (Goldston *et al.* 2016).

There are several inherent challenges with using GFRP bars as external reinforcement in concrete, which need extensive and comprehensive analysis and analyses before they can be used to replace traditional steel bars. GFRP bars are much more expensive than steel reinforcing bars at first. Glass FRP bars respond differently from standard steel bars due to their linearly elastic stress-strain behaviour up to collapse and low elastic modulus, resulting in a considerable reduction in flexural rigidity (Ascione *et al.* 2010). Moreover, GFRP reinforced flexural members experience much larger deflection/deformations under service or loading conditions as compared to steel-RC flexural members (Theriault and Benmokrane 1998). Another key concern is abrupt failure of GFRP reinforcement due to rupturing, and it is advised that they be designed as over-reinforced to promote failure by concrete crushing (ACI 2015). As a result, monitoring the crack initiation and advancement, as well as the cracking and failure mechanisms in GFRP reinforced concrete beams, is critical. In this research article a review is divide into two parts; (i) A general review of RC members reinforced with GFRP bars and (II) Review is based on the monitoring of RC structures using non-destructive acoustic emission and non-optical digital image correlation techniques.

2. RC members reinforced with GFRP bars - a review

Under four-point bending, a lot of study has been done on the performance of Simply Supported (SS) girders with internal strengthened with steel bars. The flexural behaviour of FRP reinforced concrete beams with longitudinally reinforced Glass Fibre Reinforced Polymers (GFRP) reinforcing bars was the subject of a prior study (Sam and Swamy 2005, Chitsazan *et al.* 2010, Ascione *et al.* 2010, Goldston *et al*. 2016, Goldston *et al.* 2017). Furthermore, performance and reliability and deflection computation for FRP RC beams using latest methods for an effective moment of inertia are essential issues (Rafi and Nadjai 2011) incorporating the model supplied by FRP design suggestion (ACI 2015), which is based on (Bischoff *et al.* 2009) research. Furthermore, there have been several kinds of research on the behavior of normal and high strength concrete with FRP bars, highlighting the impact of concrete strength on the performance of FRP RC beams.

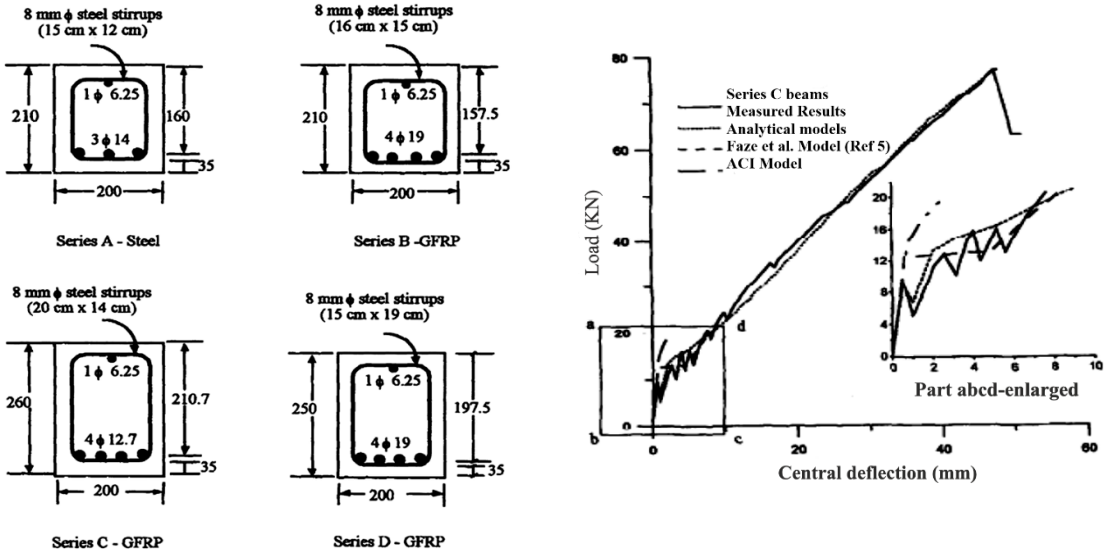

(a) (b)

Fig. 2 (a) Cross-Section and Reinforcement Details for Beams in series A, B, C, D and (b) P-Δ curve for Series C Beams (Alsayed 1998)

(Theriaule and Benmokrane 1998). The following section, which also contains a review of the research, discusses the flexural behavior, serviceability, and influence of normal concrete and high concrete strength on the performance of FRP reinforced concrete beams.

GFRP-RC beams have different flexural behavior than steel-RC beams. This is due to substantial mechanical and physical differences between GFRP and traditional steel reinforcing bars (Ascione *et al.* 2010). FRP is a linear-elastic material, whereas steel reinforcement is ductile, as previously stated. As a result, concrete crushing is the favored failure mechanism of FRP RC beams, as the beam exhibits some sort of "ductility" and plastic behavior before failure. The failure of FRP bars in tension can be catastrophic or disastrous occur without warning, thus it should be avoided (Goldston *et al.* 2016). As a result, the flexural design philosophy was developed. FRP reinforced RC beams have a different concept than typical steel RC beams. For traditional steel-reinforced concrete beams, yielding steel before exceeding the moment capacity is critical because it provides ductility and failure warning. Consequently, the FRP design procedures specify that concrete crushing govern the design for FRP reinforced concrete beams. Furthermore, as compared to steel reinforced concrete beams, FRP reinforced concrete beams exhibit substantially greater deflections and fracture widths due to mechanical characteristics, largely due to the low elasticity modulus of FRP reinforcements (Goldston *et al*. 2017). A substantial expanse of study has been done in this field by examining the flexural behavior of FRP reinforced concrete spiecemens subjected to four-point loading (Alsayed 1998, Theriaule and Benmokrane 1998, Sam and Swamy 2005, Ascione *et al.* 2010, Goldston *et al.* 2016) discussed briefly below:

Alsayed (1998) examined the flexural conduct of 12 reinforced concrete beams subjected to 4p-bending, dividing them into four groups, each with three specimens of different material characteristics. The control specimens (group A) were made using typical steel reinforcement and were meant to fail due to the steel reinforcement yielding.

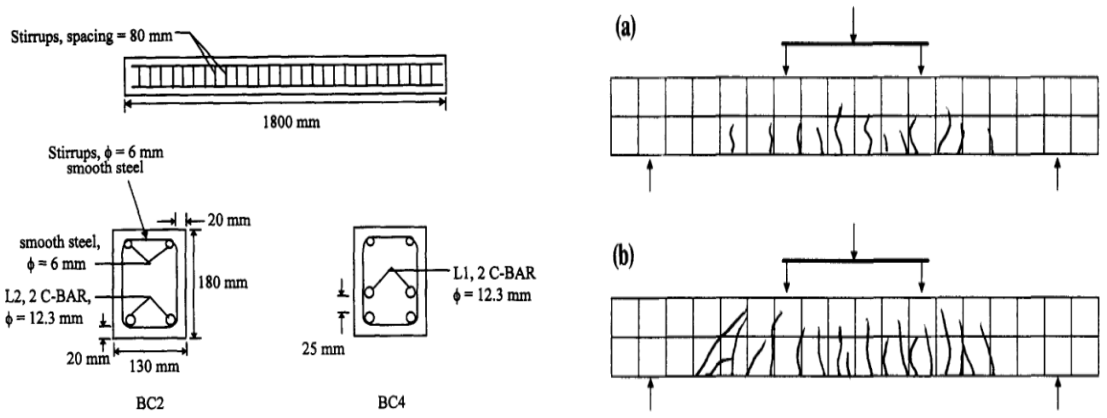

(a) (b)

Fig. 3 (a) Details of reinforcement and test specimen and (b) Cracking Pattern In BC4 and BC2 Specimen (Theriaule and Benmokrane 1998)

The remaining 9 GFRP reinforced concrete beams (groups B, C, and D) were designed to be over-reinforced with GFRP reinforcement bars, with flexural strength judged to be comparable to group one beams as shown in Fig. 2(a). The beams in the corresponding group were made in the same way. The normal strength concrete (NSC) utilized was between 31 and 41 MPa. The results of the experiments revealed that GFRP reinforcement is a viable substitute for steel reinforcement. The GFRP reinforced concrete (Series C) beams' average load-deflection behaviour showed a bi-linear correlation as shown in Fig. 2(b). The authors observed a considerable reduction in load drop near the cracking threshold, which they ascribed to the low mechanical properties (elastic modulus) of the GFRP bar. The controlled specimens were constructed as under-reinforced initially and were demonstrated to fail due to steel reinforcement giving, followed by compression failure. On the contrary, concrete crushing was the cause of the collapse because all of the GFRP RC beams were designed to be over-reinforced.

Theriaule and Benmokrane (1998) studied twelve concrete beams reinforced with E- Glass FRP bar rods were tested under 4 point loading with two different longitudinal reinforcement ratios of 1.16 percent and 2.77 percent are denoted as BC2 and BC4, respectively. The reinforcement ratio and concrete strength were two of the most important factors investigated in this research. Furthermore, the behavior of the beams was monitored before and after cracking to quantify fracture widths, crack spacing, mid-span deflections, and stresses, among other things. The ultimate moment capacity of the tested beams increases as concrete strength and reinforcement ratio increase, however, this increase is limited by the concrete compressive failure strain of over reinforced concrete beams Furthermore, when the reinforcement ratio improves, the remaining crack width, crack spacing, mid-span deflections, and stresses decrease as revealed in Fig. 3.

Sam and Swamy (2005) studied the flexural behavior of RC beams measuring (0.15 x 0.255 x 2.4) m and strengthened with Glass FRP and stainless-steel bars was evaluated under four-point loading**.** The load-carrying capacity, load-reinforcement strain, cracking, and mechanism of failure of RC beams were all examined by the author. The flexural behavior of the beam reinforced with Glass FRP bars differed from that of the beam reinforced with stainless steel bars, owing to the lower modulus of elasticity of the GFRP bars. Furthermore, the author discovered that the

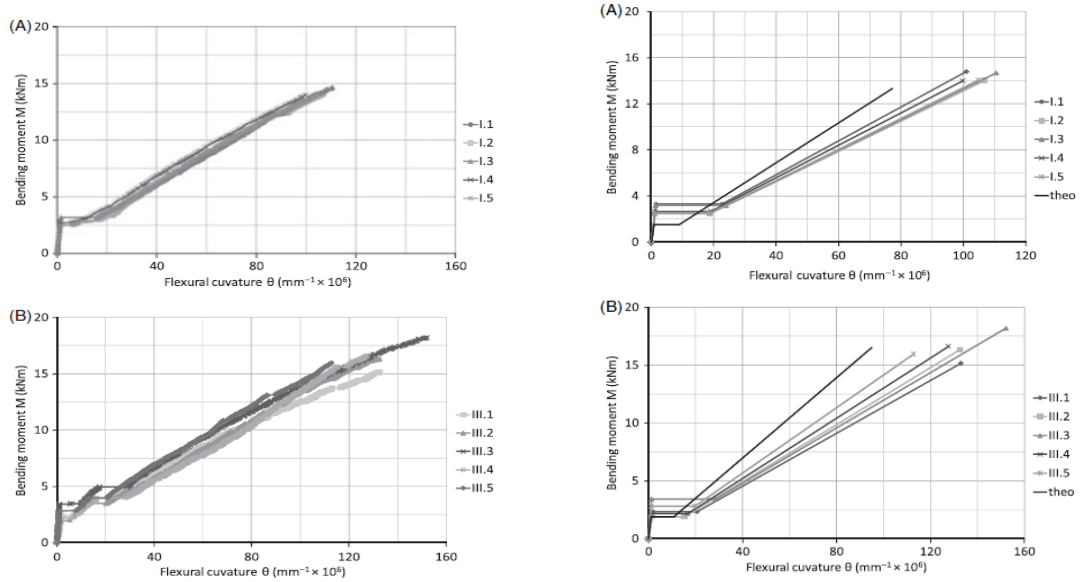

(a) (b)

Fig. 4 (a) Bending moment versus experimental flexural curvature and (b) Idealized bending moment versus experimental flexural curvature (Ascione *et al.* 2010)

deflection of the GFRP RC beam was approximately 3 times that of the traditional RC beam at the identical load level.

Ascione *et al.* (2010) examine the research observations of ten beam specimens to see what properties of concrete specimens reinforced with Glass FRP bars and stirrups are peculiar. Experimental evidence and theoretical expectations are compared as represent in Fig. 4. The author found that the moment-curvature relationship of Glass-FRP reinforced members is linear in both the pre-and-post-cracked phases; moreover, experimental results support the accuracy of the prediction formulas provided in CNR-DT 203/2006 for both deflections and crack width. RC beams strengthened by the reinforced GRP bars were examined by Kalpana and Subramanian (2011), the key factors being the strengthening ratio (1.0, 1.6, and 2.4%) and concrete compressive strength; NSC and HSC (20, 40, and 60) MPa three specimens each. Glass FRP beams dimensions were 1.8 m in length with a rectangular cross-section of (0.2 x 0.25) m subjected to 4-point bending. Steel stirrups with an 8 mm diameter and a 100 mm c/c were utilized for shear reinforcement. The P-Δ behavior, failure mechanism, and fracture breadth at various load levels were also studied. The author found that improving the ultimate load-carrying capability of the GFRP-RC beams was more important than minimizing mid-span deflection. Furthermore, for reinforcing ratios of (1.0, 1.6, and 2.4) percent, increasing concrete strength from 20 to 60 N/mm2 increased load-carrying capacities by (53, 67, and 62) percent, respectively. By maintaining concrete strength constant, load capacity increases by increasing the GFRP reinforcement ratio, whereas decreases mid-span deflection with NSC (20 N/mm2), between 3%-20%, compared to 2%-13% and 2%-7% for 40 N/mm2 and 60 N/mm2 HSC, respectively. When the GFRP reinforcement ratio was increased, while maintaining same concrete strength, the load capacity is increased, while mid-span deflection decreased by 3%-20% with NSC (20 N/mm2), compared to 2%-13% and 2%-7% for (40 and 60) N/mm2 HSC, respectively.

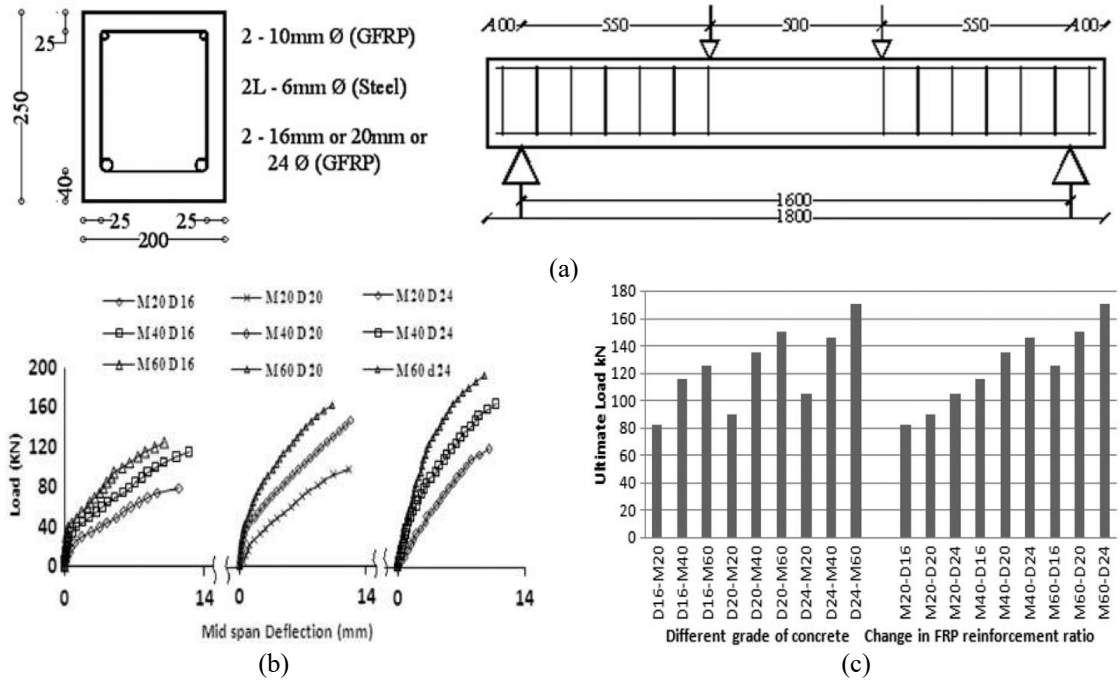

Fig. 5 (a) Cross-section detail and test setup of the beam (b) Midspan deflection of beams for varying grades of the concrete and (c) Ultimate load of GFRP beams (El-Nemr *et al.* 2013)

El-Nemr *et al.* (2013) studied the flexural behavior of twelve GFRP RC beams with normal and high strength, as well as two control specimens strengthened with conventional steel reinforcement. With cross-sectional characteristics of 0.2 m x 0.4 m and a total length of 4.25 m, the RC beams were easily supported and tested under 4-point loading. The author employs GFRP reinforcement with diverse external surface textures, such as sand coated and helically grooved. The NSC varied from 29 to 34 N/mm^2, whereas the HSC ranged from 59.1 to 73.4 N/mm^2. The major test parameters evaluated by the author were concrete compressive strength and reinforcement ratio. In comparison to NSC, the author found that GFRP-RC beams with HSC had a greater post-cracking rigidity. In comparison to the helically grooved, the sand-coated GFRP-RC beams had lower fracture widths. With both NSC and HSC, increasing the quantity of longitudinal reinforcement increased the load-carrying capability of the GFRP RC beams as shown in Fig. 5. The flexural performance of 10 GFRP reinforced RC beams was analysed by Adam *et al*. (2015) under 4-point loading. The FRP Glass RC beams had a rectangular cross-section of were 0.12 m by 0.3 m rectangular and 2.8 m long and had shear reinforcement in form of 8mm diameter steel links spaced at 150 cm/c. The concrete compressive strength (three distinct classes, including NSC (25 and 45 N/mm2) and HSC (70 N/mm2), reinforcement-ratio, and material type were all investigated by the author (GFRP reinforcement and steel reinforcement). The author discovered a bi-linear P-Δ up to catastrophe, with the crack section considerably reducing the whole stiffness of the Glass FRP reinforced concrete beams, resulting in greater deflections. Furthermore, as compared to the under-reinforced GFRP RC beams, the over-reinforced GFRP RC beams with the highest amount of tensile reinforcement showed some ductility before failure. In addition it has been found that the GFRP RC beam failure process is dependent on the tension reinforcement's

ratio. Furthermore, raising concrete strength from 25 to 45 MPa (an 80 percent increase) decreased fracture width by 52 percent, compared to an 80 percent reduction when concrete strength was raised from 25 to 70 N/mm2 (180 percent increase).

Goldston *et al*. (2016) studied the flexural behavior of GFRP-reinforced High Strength Concrete (HSC) and Ultra High Strength (UHSC) concrete beams under three-point bending, involving six beams for structural performance evaluation. The study analyzed the effects of reinforcement ratio and concrete compressive strength (HSC and UHSC) on load-carrying capacity, deflection, energy absorption, stress distribution, and failure mechanisms. Results showed that UHSC GFRP RC beams had higher energy absorption capacity than HSC GFRP RC beams. The flexural capacity of GFRP RC was conservatively estimated, with load-carrying capacity under-predicted by 36% for both HSC and UHSC beams. Furthermore, existing Glass FRP design guidelines for deflection calculations were found to be unconservative, underestimating deflections by an average of 10–22%. Further, the impact of GFRP bars as internal reinforcement on the behavior of concrete beams under four-point bending was investigated. The study considered reinforcement ratios of 0.5%, 1.0%, and 2.0% along with HSC and UHSC concrete. The P-Δ response exhibited a bi-linear trend, with the initial phase representing an uncracked beam and the latter indicating crack propagation. Over-reinforced GFRP RC beams (1.0% and 2.0% reinforcement) demonstrated reserve capacity or "ductility" before failure. Higher concrete strength significantly reduced deflection and enhanced post-cracking stiffness, with a 21% reduction in mid-span deflection at 2.0% reinforcement, compared to 7% at 1.0%. However, increasing concrete strength from normal to high had no effect on the experimental moment capacity.

Saleh *et al*. (2019) investigated the flexural behavior of eight GFRP RC beams under four-point loading. The study utilized rebars with diameters of 6.35 mm, 9.53 mm, and 12.7 mm, corresponding to reinforcement ratios of 0.5%, 1.0%, and 2.0%, respectively. The research focused on measuring and evaluating the energy absorption capacities and experimental P-Δ relationships of the beams. The author used two design codes, ACI (2015) and CSA (2012), to design GFRP-RC specimens. ACI-2015 predicted higher nominal loads, mid-span deflections, and energy absorption capacities than CSA (2012) by 20 to 43. The CSA (2012) was more conservative in these predictions. Both codes predicted values closer to experimental results for GFRP RC beams with high concrete compressive strength and tension reinforcement ratio.

Moreover, this paper examines the use of Acoustic Emission (AE) and Digital Image Correlation (DIC) techniques for monitoring cracking, damage, and fractures in steel-RC and GFRP-RC beams from crack initiation to final failure. AE, based on piezoelectric sensors, detects elastic-stress waves from crack propagation incidences, determining fracture onset and evolution based on real-time extracted parameters. (Ohno and Ohno 2010, Prem and Murthy 2017). Moreover, the severity and location of AE sources can be assessed by analyzing the AE waveform in terms of cumulative hits, amplitudes, signal strength, and time of arrival (Sharma *et al.* 2015, Sharma *et al.* 2018). Post-mortem analysis of waveform parameters helps characterize fracture mode (Sharma *et al.* 2020), while the DIC technique provides full-field, non-contact, and real-time measurements to detect cracks on a specimen's surface under loading (Bruck *et al*. 1989, Shah and Kishen 2011, Shih and Sung 2013). Cracks are characterized by discontinuities in the displacement field, allowing for the study of evolution and failure modes (De Sutter *et al.* 2017). However, this method is limited to surface measurements and cannot represent the population of cracks inside the specimen. Combining these two techniques is expected to increase structural inspection efficiency and provide regular monitoring of structures.

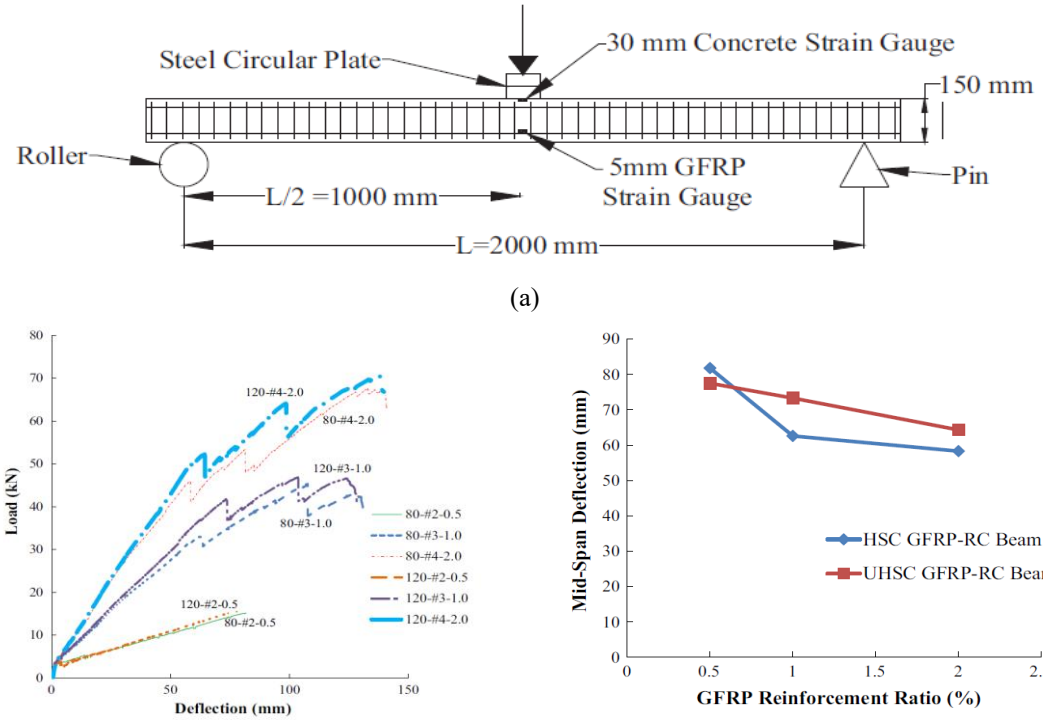

Fig. 6 (a) Schematic view of GFRP-RC beams (b) Load-midspan deflection behavior of GFRP-RC beams under static loading and (c) Effect of reinforcement ratio and concrete strength on mid-span deflection at peak 1 load (Goldston *et al*. 2017)

3. Monitoring RC Structures with AE and DIC techniques

To ensure optimal performance, a precise non-destructive method is needed to detect damage or cracks in concrete assemblies reinforced with steel or GFRP bars, using active NDT technologies like visual testing, infrared thermography, microwave, and ultrasonic testing (Sharma *et al.* 2015). However, this paper presents a passive NDT approach (Ohtsu and Tomoda 2007, Ohno and Ohtsu 2010) based on AE, a well-established and reliable method for damage detection and monitoring in reinforced concrete structures (Providakis *et al.* 2014). The AE approach offers two advantages over other non-destructive procedures: it provides critical information about internal structures and can be monitored online during structural services, making it a reliable and efficient method for assessing damage progress.

The AE approach is a method that captures the damage process, when and where it occurs, by collecting energy bursts in the form of elastic stress waves created by quick energy release during structural deflection or crack propagation. Surface-mounted AE sensors convert these transient elastic waves into electrical signals (Maji and Shah 1998, Yun *et al.* 2010), which are then used to correlate damage initiation, crack-growth, and progression in various infrastructures. Further, the AE technique is unlikely to differ from other non-destructive testing (NDT) procedures in two ways: it listens for the energy it emits and is often conducted on structures during use, as it provides sufficient loading for flaw propagation and acoustic emissions (Ohtsu and Tomoda 2007,

Ohno and Ohtsu 2010, Shah and Kishen 2012, Sharma *et al.* 2015, Prem and Murthy 2017, Garhwal *et al.* 2021). This work investigates the effectiveness of the AE technique for studying and identifying structural behavior and failure patterns of steel-RC and GFRP-RC beams.

DIC is a non-contact optical technique used to detect surface strain, displacement, and deformation in various materials (Blaber *et al.* 2015, Gribniak *et al*. 2017). This method has gained popularity for studying fracture development and material deformation due to its cost-effectiveness, ease of use, and high accuracy (Shah and Kishen 2012). DIC analyzes positional coordinates from digital images before and after deformation using cross-correlation or least-squares functions (Choi and Shah 1997, Bhowmik *et al*. 2019). This method improves structural evaluation efficiency and allows for more frequent monitoring of strength, durability, and maintenance costs during structural load testing (Blaber *et al.* 2015, Molina-Viedma *et al.* 2020). Further, this paper examines the effectiveness of AE and DIC techniques in monitoring crack initiation, propagation, and failure in steel-RC and GFRP-RC beams. By combining AE for subsurface damage detection with DIC for full-field surface deformation analysis, this approach improves structural inspection accuracy. A comprehensive review and procedural framework of these non-destructive methods are provided in Sections 4 and 5.

4. Acoustic emission technique

4.1 Basic principle

AE is the creation of elastic stress waves in a structure caused by a fast redistribution of stress or when a structure is subjected to an external stimulus such as a change in load, temperature, or pressure. Localized sources emit energy in the form of elastic-stress waves, which travel to the surface and are detected by a surface-momentum sensor (Ohstu and Tomoda 2007, Yun *et al.* 2010, Sagar and Prasad 2012). This elastic stress wave propagates through the solid due to the energy released during the bending process (Ohno and Ohno 2010, Prem and Murthy 2017). The quantity of acoustic energy emitted is determined by the magnitude and velocity of the local deformation process.

In both extremely elastic and brittle materials, AE activity can be detected (Sharma *et al*. 2015). AE has been measured and recorded in a variety of materials, including, wood, polymers, and concrete (Verbruggen *et al.* 2015). With the aid of this approach, the maintenance team may be forewarned and repair work can be completed on time, saving money on repairs and extending the life of structures (Barile *et al.* 2020). This approach has been studied for almost sixty years, and various benefits and drawbacks have been identified, some of which are described below (Ohno and Ohtsu, 2010). The technique's advantages can be summarised as follows:

- The only non-destructive approach that allows for worldwide and passive monitoring of active faults.
- Using several sensors to locate the source of AE can help and Real-time measurements are possible.
- The signals are analyzed to distinguish between real damage-related signals and background noise.

AE is the consequence of an irreversible process; therefore, any loading profile cannot be used to confirm the presence of a source in a suspected location. This characteristic, while generally beneficial, can occasionally be a barrier in testing. The tendencies for signals to attenuate, as well

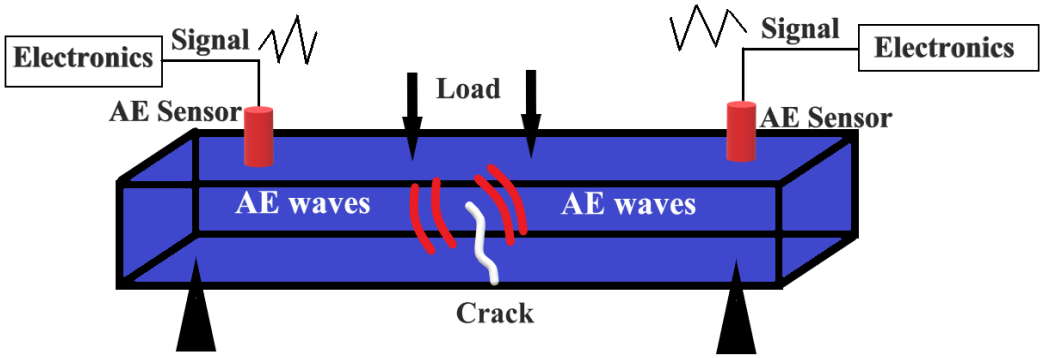

Fig. 7 Acoustic Emission Principle (Sharma *et al*. 2015)

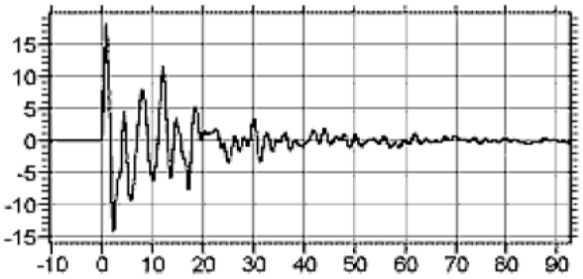

Fig. 8 Transient signal (Sharma *et al.* 2015)

as the removal of background noise, are both drawbacks of this acoustic method (Ohtsu and Tomoda 2007, Ohno and Ohtsu 2010).

4.2 Types of AE waveforms

AE is described as brief elastic-stress waves caused by the fast release of energy during mechanical loading processes in a structure or material (Ohtsu and Tomoda 2007, Ohtsu *et al.* 2011, Verbruggen *et al.* 2015). These transient elastic-stress waves propagate through the structure before being detected by acoustic sensors placed on the structure's surface. Electrical AE signals are converted from mechanical AE signals, which are then transformed into an electronic data set (Sharma *et al.* 2015). This data collection is further examined, and the collected data is graphed. The method of generating and recording acoustic emissions is depicted in Fig. 7.

In general, the following categories can be used to classify acoustic emission signals Transient Signals (Bursts): As illustrated in Fig. 8, these signals have a clear beginning and ending points that are distinct from background noise. They are frequently linked to crack propagation. Furthermore, Continuous Signal: These are never-ending waves with fluctuating amplitudes and frequencies, as the name implies. Fig. 9 depicts a typical continuous signal pattern. For motions or dislocations, they are usually the AE response.

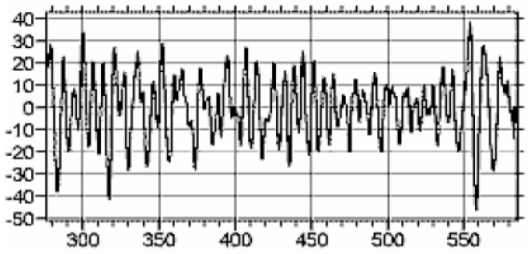

Fig. 9 Continuous signal (Sharma *et al.* 2015)

4.3 Review of AET for damage monitoring in RC beams

Maji and Shah (1988) studied the localization of cracks and movement of the Fracture Process Zone (FPZ) using the Acoustic Emission (AE) technique. Laboratory experiments were performed on plain-mortar and model-concrete specimens were subjected under direct tension and the rate of acoustic emission events and sources of AE activity were studied. The author reported that the before peak load (P_{peak}) was reached; all the recorded AE events were located near the notch. Furthermore, the author observed that a single peak load in plain-mortar specimen whereas multiple peak-load were observed in the model-concrete specimen. Moreover, the AE activity progressed during the strain-softening region with an increase in four-point loading. The FPZ was located using AE events and the location of the zone was confirmed with the location of the crack-tip evaluated by a modified Linear Elastic Fracture Mechanics (LEFM) model for plain-concrete and model concrete as well as by the microscopical observations.

Quyang *et al.* (1991) studied mode I, mode II and mixed-mode failure in pre-notched plain concrete beams specimens using the acoustic technique. Pre-notched plain concrete beams with an X-section of 0.037 m x 0.15 m were tested in the lab under 4p-loading over a span of 375 mm. AE activity in pre-notched plain concrete beams loaded in flexure using four-point loading. The acoustic emission activity was represented as mode I-II, and mixed-mode using the AE seismic moment tensor demonstration. Moreover, the author also compared the observed visual cracking on the surface of the beams. For a mode-I macro crack (center-notched), the majority of the micro-cracking or micro-crack planes were in a direction normal to the tensile stresses, where micro-cracking was rather uniformly distributed for a mode-II and mixed-mode macro-crack (off-center notched). In the end, the author also concluded that acoustic emission could be used as a powerful technique for assessing the damage in concrete as shown in Fig. 10.

Sagar *et al*. (2002) use the acoustic emission approach to describe a method for assessing damage in RC bridge beams exposed to incremental cyclic stress. The four-point loading tests were carried out on high-strength RC beams with the same reinforcement ratio (1.395%) but under three different loading circumstances (0.2115, 0.2052, and 0.1954). Three RC beams were tested, each with a depth of 0.3 m, a width of 0.15 m, and a span of 3.0 m. The concrete's compressive strength was 58 N/mm^2 after 28 days, and its tensile strength was 3.56 N/mm^2. The maximum size of coarse aggregate was 20 mm. The levels of damage indicated by AE data shift from minor to heavy damage levels as load cycles proceed, according to the author. As a result, the suggested revised criterion may be used to evaluate the damage of RC bridge beams. The author also investigates the relationship between AE activity and concrete and steel strain. Damage levels determined from maximum deflection and strain in steel and concrete are quite similar to the damage seen in RC beams, and flexure failure modes were created in RC beams.

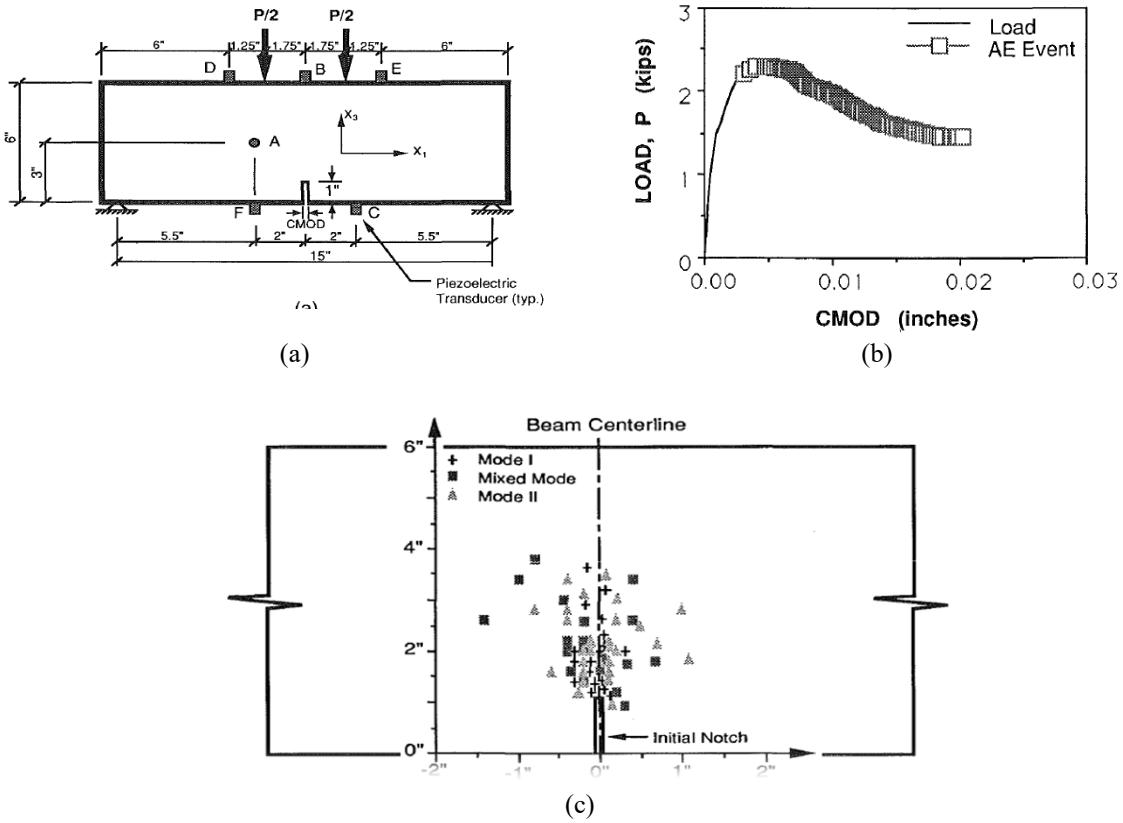

Fig. 10 (a) Geometry of Center-Notched Beam (b) Load-Crack Mouth-Opening Curve and Corresponding AE Events and (c) Locations and Fracture Modes of Microcrack for Center-Notched (Quyang *et al.* 1991)

Yun *et al*. (2010) used the acoustic emission approach to evaluate the damage of reinforced concrete beams reinforced with CFRP sheets. Five beams, each 200 mm x 300 mm in cross-section, were evaluated in the laboratory under 3-point loading across a span of 1700 mm. To serve as a reference, one of the beams was tested in its original state; the remaining 4 beams were evaluated after being reinforced using CFRP sheets glued to the tension face. Both the quantity of CFRP sheets and the number of construction imperfections were studied by the author in this investigation. For four levels of damage (I, II, III, and IV), the AE parameters in terms of AE event, amplitude, frequency, and duration time were analyzed based on initial crack, propagation, yielding of main bars, and fracture or rip-off of the CFRP sheets, and show clear differences in the different loading stages, depending on the active damage mechanism. The parameters of the average AE signal for beams reinforced with CFRP sheets, i.e., amplitude, frequency, and duration time, are in the range of 52–74 dB, 83-201 kHz, and 489-1099 μs when the crack is formed and propagated (damage levels I and II). The parameters of an average AE signal, i.e., amplitude, frequency, and duration time, were in the range of 72-89 dB, 172-230 kHz, and 891-2030 μs, respectively, when substantial fractures remained seen, major bars had surrendered (damage levels III and IV). Finally, the author found that when damage levels grow, the characteristic value of the AE signal tends to increase.

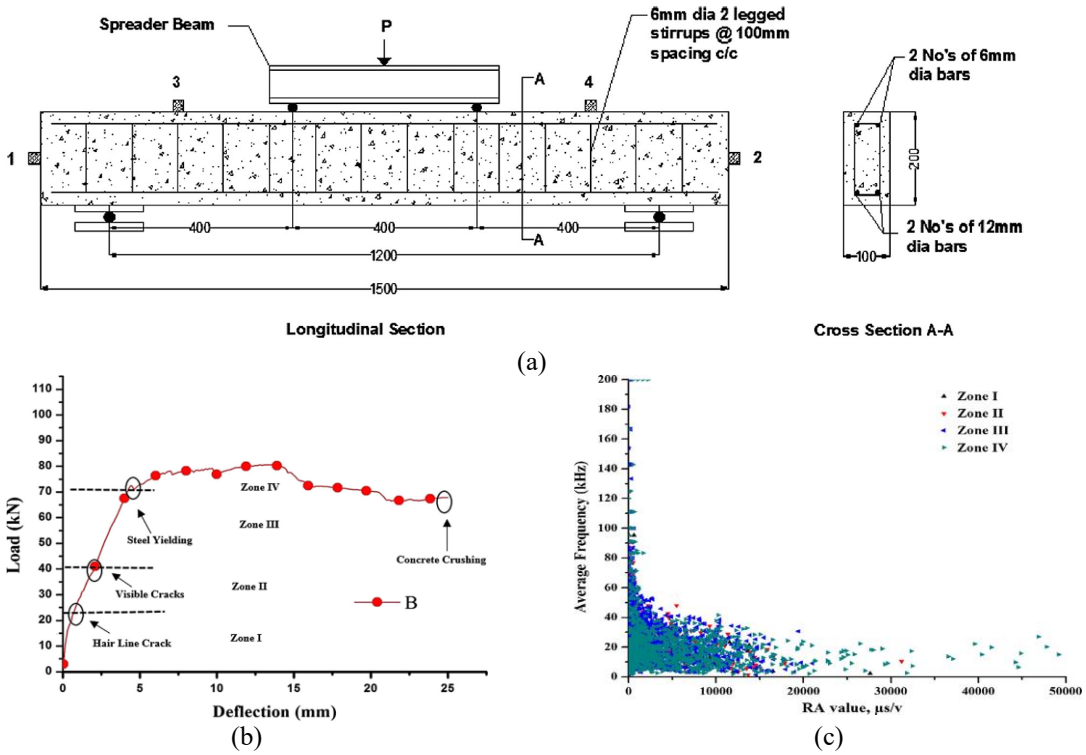

Fig. 11 (a) Under four-point bending, a typical test setup and data collection system (b) Categorization of damage zones in RC beams under bending and (c) Relation between AF and RA value of B beams (Prem and Murthy 2016)

Shahidan *et al*. (2012) studied the damage classification of RC beam utilizing AE techniques. This method was utilized to determine the extent of damage as well as the kind of damage, such as tensile and shear crack motions at key zones inside an RC beam. Laboratory experiments are performed on one type of RC beam of concrete compressive strength 35 N/mm^2 having the overall dimension of 0.15 m wide, 0.25 m depth, and 1.9 m length along with tension reinforcement i.e. 1.33% against balanced-section. The RC beam would go through four stages of mechanical behavior before failure, according to the author. These four stages are (20%, 50%, 80%) ultimate load and ultimate failure. The results were presented using an AE signal waveform such as amplitude, rise angle, average frequency, and signal strength. The result indicates high AF and low RA values are observed which implies a low level of tensile cracking at the initial stages (20% and 50% of ultimate load) in the RC beam specimen. As the load increases towards the final failure low average frequency and high RA values are noticed which implies shear movements slowly increase through the final loading stage (ultimate failure).

Prem and Murthy (2016) investigate the damage process of RC beams subjected to four-point loading. In a lab test, AE analysis is used to track the degradation of an RC beam under four-point loading. The study's major goal is to determine if AE monitoring can be used as an NDT approach in reinforced concrete structures. 3 types of reinforced concrete beams of grade M30 with overall dimensions of 0.1 m widths, 0.2 m depth, and 1.5 m length are tested in the lab against a balanced section with three different longitudinal tension reinforcements of 0.42, 0.64, and 0.93 percent and

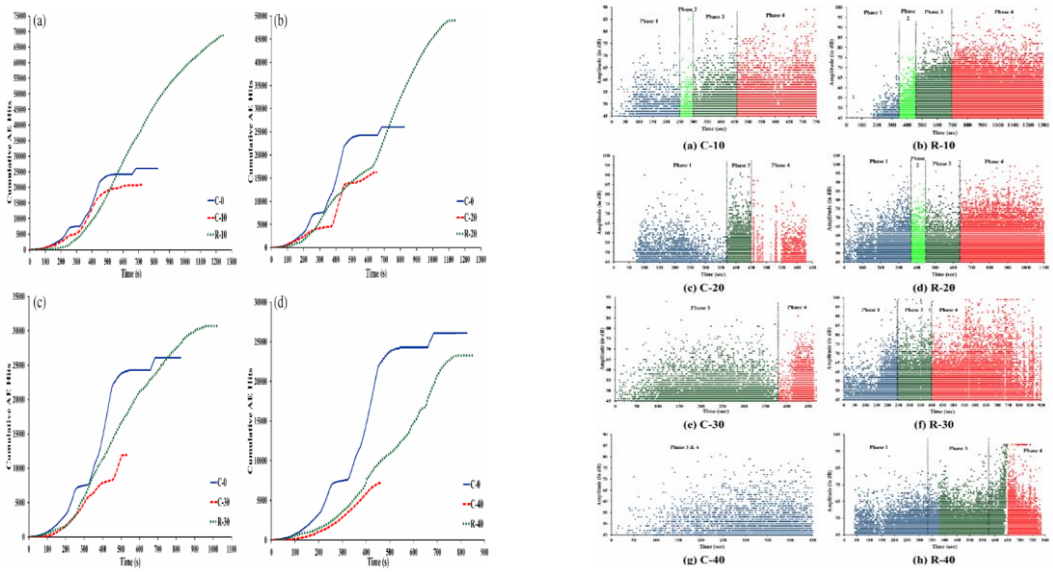

(a) (b)

Fig. 12 (a) Cumulative Hits for corroded and repaired beams;(b) Amplitude of AE hits in corroded and repaired beams (Garhwal *et al*. 2020)

it is denoted as A, B, and C Fig. 11(a). There are 4 stages of mechanical behavior the beam would experience before the collapse, according to the author. Micro cracking, localized crack propagation, widespread flexural cracking, and damage localization are the four phases. The number of counts, cumulative absolute energy, nos. of hits, and amplitude all rise as the damage level increases, as observed by the author. Furthermore, a moving average is used to do a parametric comparison between average frequency and rising angle value based on over 50 AE hits. By applying the present classification, the A, B, and C RC beams are analyzed at each level of damage. Fig. 11(b) illustrates the damage zone classification of B beams under loading and Fig. 11(c) illustrates the relation between AF and RA values of B beams. The rate of increase differs from one AE parameter to another, having amplitude having the lowest rate. Frequency varies as well, and as the level of damage increases, it decreases. The effects of longitudinal steel on all AE parameters are nearly identical, the average and cumulative values of these parameters increase as the reinforcement ratio increases (Fig. 11).

Sagar *et al.* (2017) studied the fracture monitoring of RC T-beam specimens that were put through an incremental cyclic load until they failed in bending. In a laboratory test, AE analysis is used to monitor the fracture monitoring of an RC beam under cyclic loading. Five RC flanged beams with a length of 3.2 meters and a span of 2.6 meters were tested out of which three flanged beam specimens each having 1.45 percentages of tension steel and a single specimen for test specimen containing 1.06 and 0.75 percentage of steel respectively. The total AE energy reported at the collapse of the specimen decreases as the reinforcement ratio increases, according to the author. Moreover, the author also observed that the slope of the line plotted between cumulative AE energy and time for a higher percentage of steel is less when compared with a lower percentage of steel. It might be due to the fact that the reinforcement is more the specimen may behave more brittle and fails quickly.

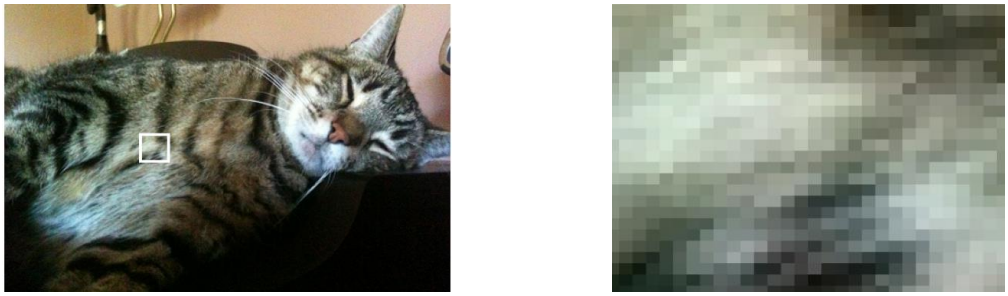

(a) (b)

Fig. 13 (a) Normal magnification digital image; (b) High magnification of a digital image (Wilbur 2011)

Garhwal *et al.* (2020) used the passive AE approach to examine the P-Δ behavior of Glass FRP repaired corroded RC beams. In the laboratory, nine beams with concrete compressive strength of 35 N/mm^2 and a cross-section of 0.127 x 0.227 m were evaluated under 4-point loads across a span of 4.1 m. The flexural performance of one control specimen with a 0.5 percent tension reinforcement ratio was used by the author. Four RC beams had different levels of corrosion (viz. C/0, C/10, C/20, C/30, and C/40). The four remaining damaged RC beam specimens (R/10, R/20, R/30, and R/40) were repaired using impressed current chloride (cl^-) induced corrosion and examined under 4p-bending. The key acoustic emission parameters explored were cumulative AE hits and amplitude versus time. According to the author, flexural testing of corroded reinforced concrete beams shows a drop in load-carrying capacity as well as a decrease in deflection as corrosion levels increase. However, when the replicates of these corroded beams were repaired with micro-concrete and Glass (FRP) covering, substantial progress in the flexural properties of the corroded beams was found, indicating that strength and integrity were restored. Because of the attenuation of the recorded AE signals produced by pre-existing cracks, the authors noticed a substantial decline in cumulative acoustic hits and their associated amplitudes as corrosion levels increased, as well as depletion of distinct AE cracking phases. As illustrated in Fig. 12, the authors also concluded that AE monitoring has the benefit of detecting the beginning and progression of damage and fractures far before they become evident on the surface, making it more desirable and useful.

5. Digitak Image Correlation (DIC)

DIC is an optical and non-contact measuring technology that allows the displacement, deformation, and strain fields of a specimen's frontal surface to be determined under any loading situation (Bruck *et al.* 1989, Wattrise *et al.* 2001, Shah and Kishen 2010, Blaber *et al.* 2015, Gribniak *et al.* 2017). The structure of a digital picture will be defined in Section 5.1 of this unit; the foundation of image matching algorithms can be established. The 2D-DIC approach will be described in Section 5.1, as well as the operational idea of the DIC measurement technique, which is how the information contained in a digital picture is utilized to monitor an object's deformation.

5.1 Structure of a digital image

Fig. 14 RGB picture with all 3 colour matrices shown and split into each colour matrix (Wilbur, 2011)

The Color Intensity (CI) of a specific spot on the surface of an object of interest is collected by rectangular arrangements of individual picture elements, in digital photographs (Choi and Shah 1997). Discrete pixels are not visible to the naked eye at normal magnification; but, as illustrated in Fig. 13(a).

In a digital photograph, the CI variations between neighboring pixels mix and appear as continuous, progressive color shifts. As seen in Fig. 13(b), increased magnification demonstrates the discrete structure of the pixel array. Color Intensity (CI) data is generally recorded as an 8-bit integer ranging from zero to 255 in each pixel of a picture (Peterson 2005, Reichmann 2011). A value of 0 implies that there is no Color Intensity (CI), whereas 255 represents the highest intensity. The Red, Green, and Blue (RGB) color space, often known as the grey scale color space, is the most popular color space utilized to capture digital pictures. Each pixel in the RGB color space has three layers of data, allowing each of the three color's intensity levels to be defined (Wilbur 2011).

Each CI matrix seems like a grey scale picture when presented separately; combining the 3 results in a full-color image, as illustrated in Fig. 14. The two most popular color spaces utilized to capture digital images are the RGB color space and the grey-scale color space (Afifi and Ashour 2012). Each pixel in the RGB color space includes three layers of data, allowing the three colors' intensity levels to be adjusted. Each colur intensity matrix will appear as a greyscale image when presented individually. A full-colored image will be generated when all three are merged, as seen in Fig. 14. Grey digital pictures are often used by DIC since just a single layer of information representing the color information on the surface of an object is needed (Maas and Hempel 2006). Grey pictures can be produced in one manner or another: by making measurements of the light intensity from the surface of an object or by scaling three RGB image CI arrangements to create a single "averaged" intensity matrix (Stevens 2007). Both options are acceptable for the use of DIC as long as the digital images have adequate changes in the intensity values of each pixel.

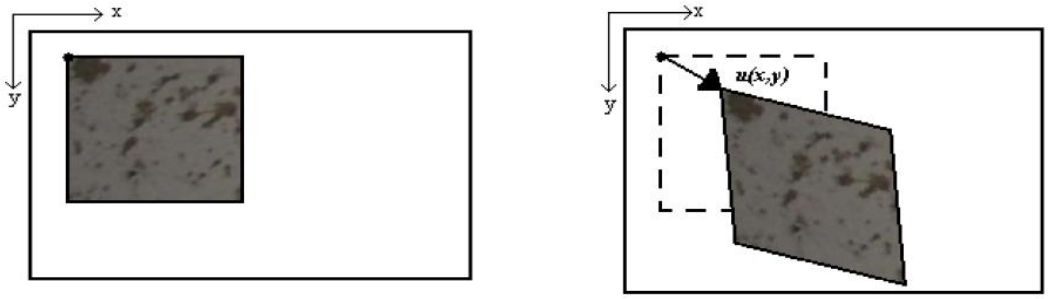

(a) (b)

Fig. 15 Illustration of a pixel subset in (a) reference position and (b) after deformation

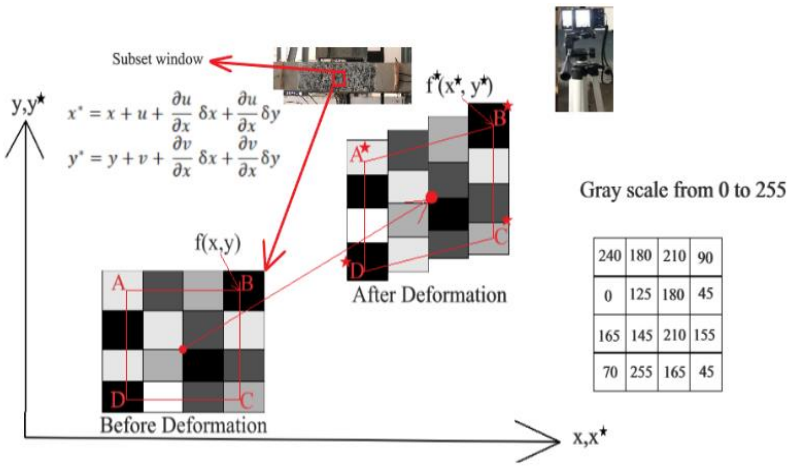

Fig. 16 Undeformed and deformed Pattern

Using a correlation criterion, every subset from the reference digital picture is identified in a digital picture of the deformed test specimen to compute the displacement of the test specimen at every load step (Pan 2018). For every subset in the deformed digital photo that the reference subset is compared to, a cross-correlation, sum-of-squared differences, or normalised cross correlation coefficient is often computed, and then the shift in the location of the subset between the two pictures is computed by identifying the maximum of the correlation coefficient matrix and computing the shift in the location of the subset between the two pictures, the displacements are calculated as shown in Fig. 13 (Bruck *et al.* 1989). These coefficients determine how comparable the two pixels being compared. A pixel subset at its reference position is illustrated in Fig. 15(a), and the same pixel subset following deformation is presented in Fig. 15(b).

To produce the full field displacement profile of a test sample, the displacement vectors obtained by correlation analysis must be interpolated. Some sub-pixel interpolation approaches that may be used to attain varying degrees of precision include genetic algorithms, intensity interpolation, and correlation coefficient curve fitting (Choi and Shah 1997). Because the members examined in the enclosed research will only be subjected to vertical forces, it is fair to infer that

displacement will only occur vertically. A discrete function expressing the grey level of every pixel describes the digital representation of the body. The grey level value runs from 0 to 255, with 0 being black and 255 indicating white, and all numbers in between indicating various shades of grey (Bruck *et al*. 1989).

As illustrated in Fig. 16, the correlation computations are performed for a group of pixels known as a pattern. Inside a pattern, the deformation field is considered to be homogenous. Before deformation, the digital picture of the body is a discrete function f(x, y), which is converted into a discrete function f*(x*, y*) after deformation (Bruck *et al.* 1989). Eq. (1) expresses the theoretical relationship between the two discrete functions.

$$f^*(x^*, y^*) - f(x + u(x, y), y + v(x, y) = 0 \tag{1}$$

Where u(x, y) and v(x, y) indicate the pattern's displacement field, as illustrated in Eq. (1).

Correlation is now simplified to the process of comparing subsets of numbers in the two digital images. Eq. (2) is used to determine the cross-correlation value, which evaluates how closely subsets match.

$$C = \frac{1-\sum[f(x,y).f^*(x^*,y^*)]}{\sum f(x,y)^2.\sum f^*(x^*,y^*)^2]^{1/2}} \tag{2}$$

f(x, y) is the grey level value at coordinate (x, y) for an undeformed photo, while f*(x*, y*) is the grey level value at point (x*, y*) for a deformed photo in Eqs. (3) and (4) The coordinates (x, y) and (x*, y*) are connected by the deformation that happened between the capture of the two digital photos. If the object's motion is parallel to the image plane in respect to the camera, then they are related by

$$x^* = x + u + \frac{\partial u}{\partial x}\delta x + \frac{\partial u}{\partial x}\delta y \tag{3}$$

$$y^* = y + v + \frac{\partial v}{\partial x}\delta x + \frac{\partial v}{\partial x}\delta y \tag{4}$$

The subset centres are displaced in the x and y axis by u and v, respectively. The letters x and y represent the distances between both the subset's centre and each point (x, y). Image correlation can be used to identify the values of coordinates (x, y), displacement (u, v), and derivatives. Detailed information about the DIC algorithms is available as open-source tools namely 2D-DIC code N-Corr (Bruck *et al*. 1989**)** operating in MATLAB.

5.2 Revies of DIC for damage monitoring in RC beams

Choi and Shah (1997) investigated the deformation of concrete subjected to compression testing is measured. The authors observed that the fractures patterns of concrete are very complicated; gages attached to the concrete specimens do not give an accurate reading. With the help of the non-contact (DIC) technique is applied to monitor the concrete fracture under compressive loads, so that gage readings are not disturbed while failure progresses. The study's major goal is to determine the viability of using DIC monitoring as a non-contact approach in concrete structures. Laboratory tests are performed on M20 grade concrete specimens with overall dimensions of 0.1 m width, 0.075 m height, and 0.075 m thickness. The prismatic shape of concrete specimens is necessary to give flat viewing frontal surfaces required for clear focusing during the digital-image grading. The author found that displacement contour maps profiles at various stages of loading were used to illustrate the development of non-uniform displacements in

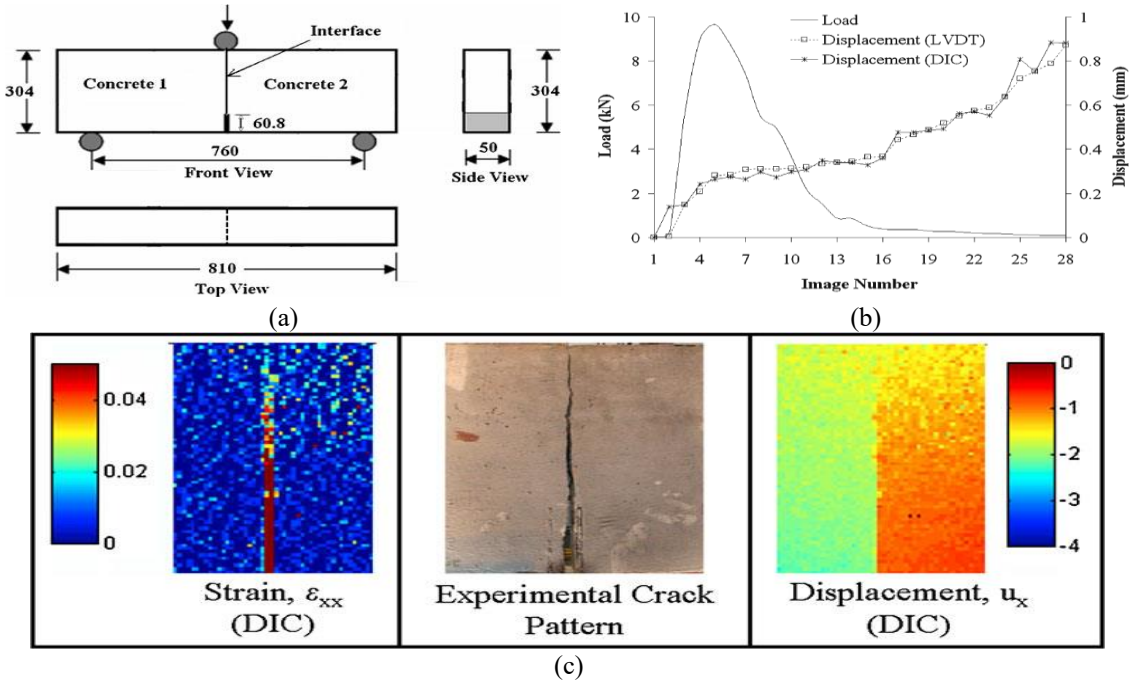

Fig. 17 (a) Geometry details of the specimen (b) Vertical load vs midspan displacement (interface beam AB) and (c) Results of strain, crack pattern, and displacement (interface beam AB) (Shah and Kishen 2010)

concrete. Authors also evaluate that with the help of this technique the cracks circumventing the aggregates and propagating parallel to the loading way in the concrete matrix.

Wattrisse *et al.* (2001) use the DIC method to perform an experimental investigation to evaluate damage in RC beams subjected to increasing cyclic stress. Laboratory experiments are performed on flat Mild steel specimens of size (77.4 x 13.9) mm. The author used a digital camera to collect surface pictures before and after the deformations, and DIC techniques were used to estimate relative motions of the points identified at the surface of interest. Additionally, the obtained digital pictures were manually adjusted to improve image quality before being input into DIC software for examination on the surface of interest. The main parameter investigated in this article was strain lagrangian strain-rate measurement (ε_{xx}) versus tensile load. The author observed that the strain-rate measurements will provide information about the onset and development of the strain localization. The author also reported that as the rate of the tensile load is small lagrangian strain-rate measurement is also small and represents with light bluish color but as tensile load is increased on flat Mild steel specimen the lagrangian strain-rate is also increased and its represents with the dark red color.

In a static test on Saint-Marcel bridge, Kuntz *et al*. (2007) studied the mechanical response of a shear crack on the RC beam. A DIC analysis of displacements was used to evaluate the mechanical conduct of a shear crack in an RC beam in response to full load cycles in static load testing. According to the author's study of displacement data, the fracture behavior changes meaningfully with load order, in this case, truck heading and position as it passes the bridge. Furthermore, a single displacement sensor does not capture tangential displacement along a fracture; at the

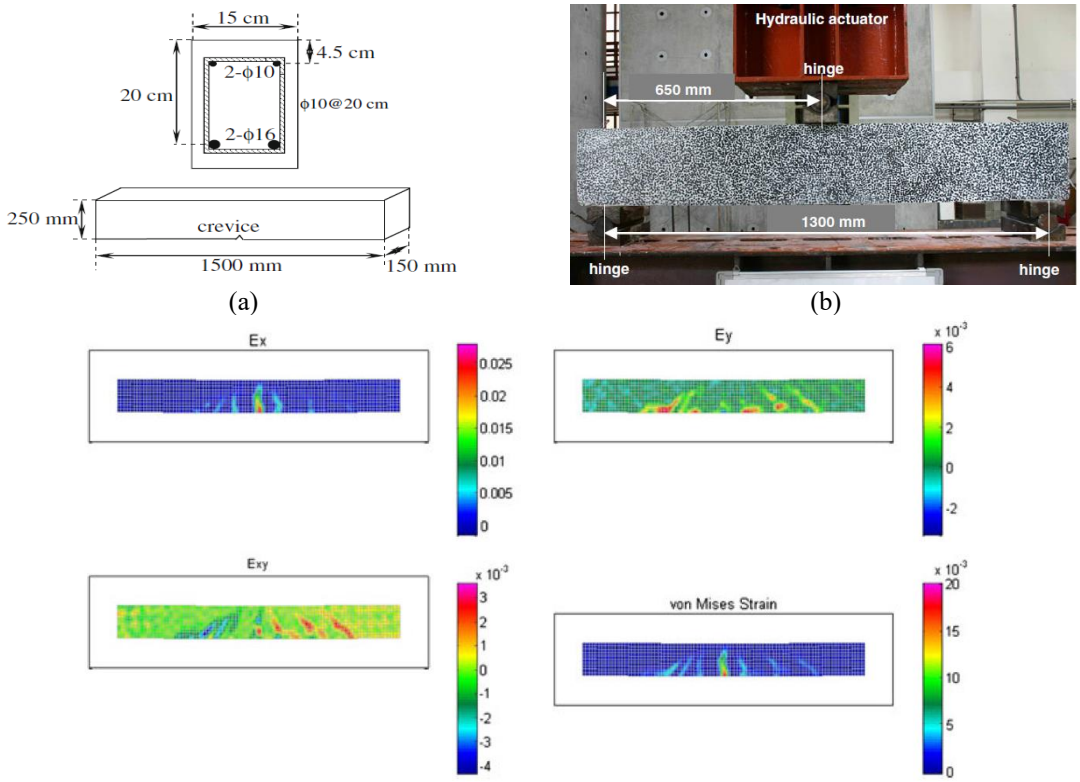

Fig. 18 (a) RC Beam dimensions of specimen 0.5% (b) Simple three-point loading set-up and (c) Strain diagram for specimen 0.5% subject to 107 kN loading (Fayyad and Lees 2014)

absolute least, two displacement transducers positioned at 90˚ to each other are required, according to the author. The correlation digital-image method gives you access to the whole displacement field, whereas two connected transducers can only provide one displacement vector. Furthermore, the final results' quality in terms of uncertainty is largely determined by the care done during the digital image capturing step.

Shah and Kishen (2010) using the Digital Image Correlation (DIC) method and a three-bending test, the fracture characteristics for various concrete-concrete surfaces were investigated. Authors capture the digital images before loading (un-deformed stage) and at different stages of loading. For the DIC analysis, the open-source code 2D-Ncorr was utilized, and the simulations were run on a personal computer. Surface displacements, surface stresses, load point displacement, Crack Mouth Opening Displacements (CMOD), and crack tip location are all determined utilizing correlation algorithms on these digital images. Vertical displacements and CMOD calculated with DIC and those obtained with Linear Variable Differential Transducers (LVDTs) and clip gauge are quite comparable, according to the author. Furthermore, the DIC method is a feasible and cost-effective alternative to LVDTs, strain gauges, and clip gauges, according to the author. In the end, the author concluded that DIC methods can successfully assess crack-tip position and crack length, which is challenging and costly for concrete-like materials using conventional sensors as presented in Fig. 17.

Sagar and Prasad (2012) studied the damage assessment of reinforced concrete (RC) beams subjected to incremental cyclic loading under four-point loading. The combined techniques of AE and DIC to assess the damage in reinforced concrete beams subjected to incremental cyclic loading. The main idea was to study damage assessment in RC beams was studied according to different limit states specified by the code of practice IS-456:2000. Experiments are conducted in the laboratory utilizing RC beams of 58 Mpa compressive strength along with overall dimensions of 0.15m and 0.30 m i.e., width and depth, and 3.2m length, as well as longitudinal tension reinforcement of 1.39%, and four-point loading. Author observed that the during the fracture process of RC beams the damage levels qualified by AE data shifts from minor to major levels as the strain in steel and concrete increases. DIC technique is useful to record strain in concrete structures remotely without hindering the usage. The combination of AE and DIC techniques has the potential to provide the state of damage in RC structures effectively.

Fayyad and Lees (2014) under three-point loading, the fracture monitoring of steel-reinforced concrete specimens was investigated. Digital image correlation (DIC) is utilised for a laboratory test to monitor the fracture control of the loaded steel RC beam. The study's main goal is to use DIC to analyze mode-I fracture propagation in reinforced concrete structures (see Fig. 18.). In laboratory tests, two types of RC beams were utilized, with concrete compressive strengths of 36 and 46 N/mm2, overall dimensions of 0.1m width, 0.12 m depth, and 0.84 m length, and two distinct longitudinal tension reinforcement ratios of 0.5 percent. The displacement vectors of the DIC analysis findings were used to calculate the CMOD values for the investigated samples, which was the major parameter addressed in this research. The DIC analysis was carried out using an open-source tool called GeoPIV, and the simulations were run on a personal computer. CMOD was made on the basis of the DIC analysis and the concrete strength was revealed to have minimal effect on the opening of cracks; but the binding stresses between the reinforcement and the concrete seemed to have a role in the propagation of fractures and the breaking through of cracks. Researchers may also view and evaluate the fracture characteristics of RC beams using the DIC method.

Using the DIC technique, Hamrat *et al.* (2015) examine cracking behaviour of both conventional and high-force concrete and high-force fibre concrete beams. Three flexural reinforcement ratios of 1.22%, 1.77%, and 2.42% were used for each series of beams. The beams were 1.5 m long and had a cross-section of 0.1 m x 0.16 m. Beams were subjected to a symmetric loading composed of 4p-loading. The main parameters investigated in this article were crack detection, crack development, crack width measurements, and surface strain. The load-carrying capacity of concrete beams improves as the percentage of tensile reinforcement and compressive strength increases, according to the author. The comparison between standard measuring techniques (strain gauges, LVDT sensors) and the DIC approach was assessed by the author. The measurement of strains and displacements at or near failure, according to the author, is generally not feasible using normal methods, because of the safety risk and damage to equipment. In addition, the good agreement between the two metering methods shows that the DIC methodology is an effective tool for monitoring displacement and stress areas throughout loading from beginning to failure.

Tambusay *et al.* (2018) under three-point bending, study the shear fracture mechanism of RC beams is investigated by the author. DIC analysis is used to visualize the formation and propagation of shear cracking behavior in an RC beam in a laboratory test. In the lab, three types of M30 RC beams with overall dimensions of 0.1 m width, 0.125 m effective depth, and 1.0 m length are evaluated against a balanced section with longitudinal tension reinforcement of 2.4

percent. According to the author, the suggested DIC system has enough resolution to monitor the onset and development of shear cracking in an RC beam. Furthermore, DIC findings revealed that concrete cracking appears as a succession of thin, high-strain strips. With increasing loading, the amount of strain increases, suggesting an increase in fracture width. In this work, hand-drawn crack maps and nonlinear finite element analysis strain fields ($\boldsymbol{\varepsilon}_{xx}$) compare favourably to strain fields ($\boldsymbol{\varepsilon}_{xx}$) created using the DIC approach, in this study. According to the author, DIC is also proving to be a useful technique for studying many aspects of the shear failure process in RC.

Bhowmik *et al.* (2019) under the influence of static loading, a variety of small, medium, and large concrete beams were tested. The DIC method has been used to study concrete fracture mechanisms and crack development characteristics. Three distinct types of concrete beams with concrete compressive strength of 34.50 N/mm^2 and total dimensions of 400 mm span, 550 mm length, 20 mm notch size, and 100 mm depth is tested in the lab. Surface displacements, surface strains, CMOD, and crack tip position are calculated using VIC-2D software to examine digital pictures. Digital images corresponding to peak load, 90% post-peak load, 70% post-peak load, 50% post-peak load, 30% post-peak load, and 15% post-peak load were selected for the beam specimens under static loading. The vertical displacements produced from the 2D-DIC analysis were compared to experimental data under static loading conditions at various percentages of post-peak load. Vertical displacements produced by 2D-DIC have also been compared to experimental results in fatigue loading scenarios. The authors discovered a strong correlation between the findings of the DIC analysis and the experimentally observed values.

Johansson *et al*. (2020) studied the residual capacity in RC beams subjected to impact loading under three-point loading. DIC analysis is used to visualize and study the structural response of impact-loaded concrete beams. The main idea was to study the residual plastic deformation capacity of RC beams first subjected to impact loading, and this was done with high accuracy using DIC analysis. With a span of 1000 mm and dimensions of (0.1 x 0.1 x 1.18) m, the beams were simply supported. The drop weight had a mass of 10 kg and was dropped from heights 2500 mm. A high-speed resolution camera, with 5000 fps, was used during the impact tests. From the digital images obtained, (DIC) analyses were conducted, and deformations and crack propagation of the RC beams were measured. The author observed that the deformations were obtained well, and the largest cracks were acceptably captured, but the smaller cracks were not observed using DIC. Furthermore, DIC analysis can detect and identify early crack deformations as well as crack propagation in RC beams.

Moreover, Few researchers have suggested combining AE and DIC for structural damage assessment. Sagar and Prasad (2012) used AE and DIC techniques to assess damage in reinforced concrete beams subjected to incremental cyclic loading. They also suggested characterizing damage mechanisms during bending failure of different types of concrete beams reinforced by composite materials (Aggelis *et al.* 2013, Verbruggen *et al*. 2014, Verbruggen *et al*. 2016) Furthermore, the combined use of AE and DIC has been applied in tensile-loading tests of fiber-reinforced mortar samples (Rouchier *et al*. 2013). More recently, this methodology has been utilized to analyze the fracture process zone, cracking mechanisms, and size effects in notched plain concrete beams. Building on these applications, the authors propose integrating AE and DIC for fracture analysis of concrete beams reinforced with steel and GFRP bars. While AE provides insights into both volumetric and surface effects, its visualization accuracy is limited (Agglies *et al.* 2013). In contrast, DIC offers high-precision full-field displacement mapping but is restricted to surface measurements (Pan 2018).

Sharma *et al.* 2021 examined the flexure behavior and cracking pattern of RC beams with steel

and GFRP reinforcement. The beams were cast with dimensions of 150 x 230 x 2100 mm and designed according to ACI 319 (2019) and ACI Committee 440 (2015) codes. The beams had longitudinal and transverse reinforcement ratios of 0.33%, 0.52%, and 1.11%. The study found that the ultimate load-carrying capacity increases with tensile reinforcement in both steel and GFRP reinforced concrete beams. The AE waveform parameters, amplitude and number of AE hits, accurately correlate cracking initiation and progression. GFRP-RC beams show 20-30% more AE activity than steel-RC beams due to their lower modulus of elasticity, resulting in larger ductility and deflections. Furthermore, the use of AE XY event plots and longitudinal strain profiles using DIC provides real-time visual representations of progressive AE activity and strains in steel-RC and GFRP-RC beams. These methods closely match the observed micro- and macro-cracks in the actual beams at different loading stages (Sharma *et al.* 2020, Sharma *et al.* 2021). The integration of these techniques could lead to more comprehensive non-destructive monitoring tools in RC structures, making them more quantitative and effective.

6. Conclusions

The primary objective of this study was to evaluate and synthesize existing research on FRP-reinforced concrete beams monitored using AE and DIC techniques, with a particular focus on their flexural behavior. This review highlights the well-established relationships between the mechanical and non-mechanical properties of FRP RC members. However, notable inconsistencies were identified. Unlike steel reinforcement, the "surface deformation" of FRP bars was found to have no direct correlation with their mechanical properties.

Furthermore, the sudden brittle failure of GFRP RC structures necessitates an effective real-time structural health monitoring strategy to assess integrity, performance, and crack propagation before catastrophic failure occurs. Although numerous international codes and guidelines exist for FRP-reinforced structures, India currently lacks standardized design practices. With further research and standardization, FRP bars could serve as a viable alternative to traditional steel reinforcement.

From a technological perspective, the combination of AE and DIC provides complementary insights AE serves as the "ear" detecting crack initiation and propagation, while DIC functions as the "eye" capturing strain distribution and displacement patterns. AE effectively identifies the onset and progression of cracks but offers limited information about damage severity, as indicated by AE signal amplitude. On the other hand, DIC, acting as a virtual extensometer, enables displacement measurements at designated points, reducing reliance on conventional LVDTs and strain gauges. However, its accuracy is influenced by image quality, dust accumulation on the testing surface, and lens specifications.

Integrating these two techniques enhances their individual capabilities, with DIC validating AE observations by correlating strain field variations with AE-recorded emissions. Consequently, AE-DIC integration presents a promising non-destructive approach for real-time monitoring and mapping of fracture progression in both steel- and GFRP-reinforced concrete structures.

Despite its potential, the AE-DIC approach has certain limitations that must be addressed to improve its effectiveness in real-world structural health monitoring applications. Environmental factors, such as humidity, temperature fluctuations, and surface conditions, can impact DIC accuracy due to variations in lighting and dust accumulation. AE signal interpretation remains a challenge, as distinguishing between microcracking, fiber rupture, and delamination in FRP

requires advanced signal processing and expert analysis. Additionally, the high-speed cameras required for DIC and the sensitivity demands of AE transducers contribute to increased costs and setup complexity, limiting widespread adoption.

To overcome these challenges, future research should focus on refining sensor technologies, enhancing data integration methods, and developing cost-effective solutions. Advancements in AI-driven signal processing and automation could further improve the reliability and practicality of AE-DIC systems, making them a scalable and robust solution for structural health monitoring.

References

ACI Committee (2015), Guide for the Design and Construction of Structural Concrete Reinforced with Fiber-Reinforced Polymer Bars. ACI440. 1R-15, American Concrete Institute, Farmington Hills, MI, 88(2), 546-565.

Adam, M.A., Said, M., Mahmoud, A.A. and Shanour, A.S. (2015), "Analytical and experimental flexural behavior of concrete beams reinforced with glass fiber reinforced polymers bars", *Constr. Build. Mater.*, **84**, 354-366. https://doi.org/10.1016/j.conbuildmat.2015.03.057.

Aggelis, D.G., Verbruggen, S., Tsangouri, E., Tysmans, T. and Van Hemelrijck, D. (2013), "Characterization of mechanical performance of concrete beams with external reinforcement by acoustic emission and digital image correlation", *Constr. Build. Mater.*, **47**, 1037-1045. https://doi.org/10.1016/j.conbuildmat.2013.06.005.

Allahvirdizadeh, R., Rashetnia, R., Dousti, A. and Shekarchi, M. (2011), "Application of polymer concrete in repair of concrete structures: A literature review", *Concrete Solutions*, 435-444.

Alsayed, S.H. (1998), "Flexural behaviour of concrete beams reinforced with GFRP bars", *Cement Concrete Compos.*, **20**(1), 1-11.

Barile, C., Casavola, C., Pappalettera, G. and Kannan, V.P. (2020), "Application of different acoustic emission descriptors in damage assessment of fiber reinforced plastics: A comprehensive review", *Eng. Fract. Mech.*, **235**, 107083. https://doi.org/10.1016/j.engfracmech.2020.107083.

Bhowmik, S., Dubey, S. and Ray, S. (2019), "Investigation on fracture processes of concrete", *Frattura ed Integrità Strutturale*, **13**(48), 419-428. https://doi.org/10.3221/IGF-ESIS.48.40.

Blaber, J., Adair, B. and Antoniou, A. (2015), "Ncorr: open-source 2D digital image correlation matlab software", *Exp. Mech.*, **55**(6), 1105-1122. https://doi.org/10.1007/s11340-015-0009-1.

Bruck, H.A., McNeill, S.R., Sutton, M.A. and Peters, W.H. (1989), "Digital image correlation using Newton-Raphson method of partial differential correction", *Exp. Mech.*, **29**(3), 261-267. https://doi.org/10.1007/BF02321405.

Chitsazan, I., Kobraei, M., Jumaat, M.Z. and Shafigh, P. (2010), "An experimental study on the flexural behaviour of FRP RC bemas and comparison of the ultimate moment capacity with ACI", *J. Civil Eng. Constr. Tech.*, **1**(2), 27-42.

Choi, S. and Shah, S.P. (1997), "Measurement of deformations on concrete subjected to compression using image correlation", *Exp. Mech.*, **37**(3), 307-313. https://doi.org/10.1007/BF02317423.

De Sutter, S., Verbruggen, S., Tysmans, T. and Aggelis, D.G. (2017), "Fracture monitoring of lightweight composite-concrete beams", *Compos. Struct.*, **167**, 11-19. https://doi.org/10.1016/j.compstruct.2017.01.024.

Dhawan, S.K., Bindal, A., Bhalla, S. and Bhattacharjee, B. (2019), "Expected residual service life of reinforced concrete structures from current strength considerations", *Adv. Struct. Eng.*, 22(7), 1631-1643. https://doi.org/10.1177/1369433218818001.

El Maaddawy, T., Soudki, K. and Topper, T. (2005), "Long-term performance of corrosion-damaged reinforced concrete beams", *ACI Struct. J.*, **102**(5), 649.

El-Hacha, R., Mirmiran, A., Cook, A. and Rizkalla, S. (2011), "Effectiveness of surface-applied corrosion inhibitors for concrete bridges", *J. Mater. Civil Eng.*, **23**(3), 271-280.

https://doi.org/10.1061/(ASCE)MT.1943-5533.0000163.
Francois, R. and Maso, J.C. (1988), "Effect of damage in reinforced concrete on carbonation or chloride penetration", *Cement Concrete Res.*, **18**(6), 961-970. https://doi.org/10.1016/0008-8846(88)90033-6.
Garhwal, S., Sharma, S. and Sharma, S.K. (2021), "Monitoring the flexural performance of GFRP repaired corroded reinforced concrete beams using passive acoustic emission technique", *Struct. Concrete*, **22**(1), 198-214. https://doi.org/10.1002/suco.202000247.
Goldston, M.W., Remennikov, A. and Sheikh, M.N. (2017), "Flexural behaviour of GFRP reinforced high strength and ultra high strength concrete beams", *Constr. Build. Mater.*, **131**, 606-617. https://doi.org/10.1016/j.conbuildmat.2016.11.094.
Goldston, M., Remennikov, A. and Sheikh, M.N. (2016), "Experimental investigation of the behaviour of concrete beams reinforced with GFRP bars under static and impact loading", *Eng. Struct.*, **113**, 220-232. https://doi.org/10.1016/j.engstruct.2016.01.044.
Hansson, C.M. (1995), "Concrete: the advanced industrial material of the 21st century", *Metallurgical and Mater. Trans. B*, **26**(3), 417-437. https://doi.org/10.1007/BF02653859.
Hensher, D.A. (2016), *Fiber-reinforced-plastic (FRP) reinforcement for concrete structures: properties and applications* (Vol. 42). Elsevier.
Lee, S.K., Krauss, P.D. and Wiss, J. (2004), *Long-term performance of epoxy-coated reinforcing steel in heavy salt-contaminated concrete* (No. FHWA-HRT-04-090). United States. Federal Highway Administration. Office of Infrastructure Research and Development.
Mancusi, G. and Spadea, S. (2010), "Flexural behaviour of concrete beams reinforced with GFRP bars", *Strain*, **46**(5), 460-469. https://doi.org/10.1111/j.1475-1305.2009.00662.x.
Manning, D.G. (1996), "Corrosion performance of epoxy-coated reinforcing steel: North American experience", *Constr. Build. Mater.*, **10**(5), 349-365. https://doi.org/10.1016/0950-0618(95)00028-3.
Ohno, K. and Ohtsu, M. (2010), "Crack classification in concrete based on acoustic emission", *Constr. Build. Mater.*, **24**(12), 2339-2346. https://doi.org/10.1016/j.conbuildmat.2010.05.004.
Ohtsu, M. and Tomoda, Y. (2007), "Corrosion process in reinforced concrete identified by acoustic emission", *Mater. Trans.*, **48**(6), 1184-1189. https://doi.org/10.2320/matertrans.I-MRA2007844.
Ohtsu, M. and Uddin, F. A. (2008), "Mechanisms of corrosion-induced cracks in concrete at meso-and macro-scales", *J. Adv. Concrete Tech.*, **6**(3), 419-429. https://doi.org/10.3151/jact.6.419.
Ohtsu, M., Mori, K. and Kawasaki, Y. (2011), "Corrosion process and mechanisms of corrosion-induced cracks in reinforced concrete identified by AE analysis", *Strain*, **47**, 179-186. https://doi.org/10.1111/j.1475-1305.2010.00754.x.
Pan, B. (2018), "Digital image correlation for surface deformation measurement: historical developments, recent advances and future goals", *Measurement Sci. Technol.*, **29**(8), 082001.
Prem, P.R. and Murthy, A.R. (2017), "Acoustic emission monitoring of reinforced concrete beams subjected to four-point-bending", *Appl. Acoust.*, **117**, 28-38. https://doi.org/10.1016/j.apacoust.2016.08.006.
Providakis, C.P., Stefanaki, K.D., Voutetaki, M.E., Tsompanakis, Y. and Stavroulaki, M. (2014), "Damage detection in concrete structures using a simultaneously activated multi-mode PZT active sensing system: Numerical modelling", *Struct. Infrastruct. Eng.*, **10**(11), 1451-1468. https://doi.org/10.1080/15732479.2013.831908.
Rabi, M., Cashell, K.A. and Shamass, R. (2019), "Flexural analysis and design of stainless steel reinforced concrete beams", *Eng. Struct.*, **198**, 109432. https://doi.org/10.1016/j.engstruct.2019.109432.
Rouchier, S., Foray, G., Godin, N., Woloszyn, M. and Roux, J.J. (2013), "Damage monitoring in fibre reinforced mortar by combined digital image correlation and acoustic emission", *Constr. Build. Mater.*, **38**, 371-380. https://doi.org/10.1016/j.conbuildmat.2012.07.106.
Saleh, Z., Goldston, M., Remennikov, A.M. and Sheikh, M.N. (2019), "Flexural design of GFRP bar reinforced concrete beams: An appraisal of code recommendations", *J. Build. Eng.*, **25**, 100794. https://doi.org/10.1016/j.jobe.2019.100794.
Sam, A.R.M. and Swamy, R.N. (2005), "Flexural behavior of concrete beams reinforced with glass fiber reinforced polymer bars", *Malaysian J. Civil Eng.*, **17**(1), 49-57. https://doi.org/10.11113/mjce.v17.15672.
Shah, S.G. and Kishen, J.C. (2011), "Fracture properties of concrete–concrete interfaces using digital image

correlation", *Exp. Mech.*, **51**(3), 303-313. https://doi.org/10.1007/s11340-010-9358-y.
Shah, S.G. and Kishen, J.C. (2012), "Use of acoustic emissions in flexural fatigue crack growth studies on concrete", *Eng. Fract. Mech.*, **87**, 36-47. https://doi.org/10.1016/j.engfracmech.2012.03.001.
Sharma, G., Sharma, S. and Sharma, S.K. (2020), "Monitoring structural behaviour of concrete beams reinforced with steel and GFRP bars using acoustic emission and digital image correlation techniques", *Struct. Infrastruct. Eng.*, 1-16. https://doi.org/10.1080/15732479.2020.1836661.
Sharma, G., Sharma, S. and Sharma, S.K. (2021), "Fracture monitoring of steel and GFRP reinforced concrete beams using acoustic emission and digital image correlation techniques", *Struct. Concrete*, **22**(4), 1962-1976. https://doi.org/10.1002/suco.202000650.
Sharma, G., Sharma, S. and Sharma, S.K. (2021), "Non-destructive evaluation of steel and GFRP reinforced beams using AE and DIC techniques", **77**(5), 637-650. https://doi.org/10.12989/sem.2021.77.5.637.
Shih, M.H. and Sung, W.P. (2013), "Application of digital image correlation method for analysing crack variation of reinforced concrete beams", *Sadhana*, **38**(4), 723-741. https://doi.org/10.1007/s12046-013-0141-5.
Stankiewicz, A., Szczygieł, I. and Szczygieł, B. (2013), "Self-healing coatings in anti-corrosion applications", *J. Mater. Sci.*, **48**(23), 8041-8051. https://doi.org/10.1007/s10853-013-7616-y.
Tambusay, A., Suryanto, B. and Suprobo, P. (2018), "Visualization of shear cracks in a reinforced concrete beam using the digital image correlation", *Int. J. Adv. Sci. Eng. Inform. Technol.*, **8**(2), 573-578. https://doi.org/10.18517/ijaseit.8.2.4847.
Theriault, M. and Benmokrane, B. (1998), "Effects of FRP reinforcement ratio and concrete strength on flexural behavior of concrete beams", *J. Compos Constr.*, **2**(1), 7-16. https://doi.org/10.1061/(ASCE)1090-0268(1998)2:1(7).
Verbruggen, S., Aggelis, D.G., Tysmans, T. and Wastiels, J. (2014), "Bending of beams externally reinforced with TRC and CFRP monitored by DIC and AE", *Compos. Struct.*, **112**, 113-121. https://doi.org/10.1016/j.compstruct.2014.02.006.
Verbruggen, S., De Sutter, S., Iliopoulos, S., Aggelis, D.G. and Tysmans, T. (2016), "Experimental structural analysis of hybrid composite-concrete beams by digital image correlation (DIC) and acoustic emission (AE)", *J. Nondestruct. Eval.*, **35**(1), 2. https://doi.org/10.1007/s10921-015-0321-9.
Vidya Sagar, R., Raghu Prasad, B.K. and Sharma, R. (2012), "Evaluation of damage in reinforced concrete bridge beams using acoustic emission technique", *Nondestructi. Test. Eval.*, **27**(2), 95-108. https://doi.org/10.1080/10589759.2011.610452.
Wattrisse, B., Chrysochoos, A., Muracciole, J.M. and Némoz-Gaillard, M. (2001), "Analysis of strain localization during tensile tests by digital image correlation", *Exp. Mech.*, **41**(1), 29-39. https://doi.org/10.1007/BF02323101.
Wilbur, P.C. (2011), *Damage Identification in Reinforced Concrete Beams using Digital Image Correlation*. University of Windsor (Canada).
Yun, H.D., Choi, W.C. and Seo, S.Y. (2010), "Acoustic emission activities and damage evaluation of reinforced concrete beams strengthened with CFRP sheets", *NDT & E Int.*, **43**(7), 615-628. https://doi.org/10.1016/j.ndteint.2010.06.006.

JK